First-principles reinvestigation of bulk WO₃

Hanen Hamdi,[1] Ekhard K. H. Salje,[2] Philippe Ghosez,[1] and Eric Bousquet[1]

[1]*Theoretical Materials Physics, Q-MAT, CESAM, Université de Liège, B-4000 Sart Tilman, Belgium*

[2]*Department of Earth Sciences, University of Cambridge, Downing Street, Cambridge CB2 3EQ, England, United Kingdom*

Using first-principles calculations, we analyze the structural properties of tungsten trioxide WO₃. Our calculations rely on density functional theory and the use of the B1-WC hybrid functional, which provides very good agreement with experimental data. We show that the hypothetical high-symmetry cubic reference structure combines several ferroelectric and antiferrodistortive (antipolar cation motions, rotations, and tilts of oxygen octahedra) structural instabilities. Although the ferroelectric instability is the largest, the instability related to antipolar W motions combines with those associated to oxygen rotations and tilts to produce the biggest energy reduction, yielding a $P2_1/c$ ground state. This nonpolar $P2_1/c$ phase is only different from the experimentally reported Pc ground state by the absence of a very tiny additional ferroelectric distortion. The calculations performed on a stoichiometric compound so suggest that the low-temperature phase of WO₃ is not intrinsically ferroelectric and that the experimentally observed ferroelectric character might arise from extrinsic defects such as oxygen vacancies. Independently, we also identify never observed $R3m$ and $R3c$ ferroelectric metastable phases with large polarizations and low energies close to the $P2_1/c$ ground state, which makes WO₃ a potential antiferroelectric material. The relative stability of various phases is discussed in terms of the anharmonic couplings between different structural distortions, highlighting a very complex interplay.

I. INTRODUCTION

Tungsten trioxide, WO₃, has been extensively studied due to its very attractive and rich properties for technological applications. WO₃ and its derivatives H_xWO_3 and WO_{3-x} are electrochromic [1–6], thermochromic [7,8], and superconducting [3,8–14]. It has been envisaged that WO₃ may become one of the best materials for electrochromic applications such as in energy-efficient windows, smart glasses, antiglare automobile rear-view mirrors, sunroofs, displays, or even tunable photonic crystals [15] and to reduce photocorrosion [16]. The wide variety of the underlying electronic instabilities for these properties is mirrored by a multitude of related structural instabilities, which have been investigated ever since 1975 [17,18] and refined later [19–24].

All known WO₃ phases are characterized by very large distortions of the archetypal perovskite structure so that even the notion of octahedra tilts is to be taken with some caution. The WO₆ octahedra are so largely distorted that the variance of W–O distances in any observed structure is far greater than in most other known perovskite structures [25–29]. In this paper we make the fundamental connection between the electronic and structural structure properties of WO₃ and show that most, if not all, structural instabilities can be derived from a careful analysis of its intrinsic cubic phonon instabilities, despite these large deformation amplitudes.

The structural properties can be summarized as follows: WO₃ shows no proper melt; surface melting of crystalline material occurs at 1746 K. Crystal growth proceeds typically by sublimation and gas transport at temperatures below 1400 K. At the highest temperatures the structure is tetragonal (space group $P4/nmm$) with strong antiferrodistortive cation movements so that the WO₆ octahedra are strongly distorted [30] in an antipolar pattern. Additional rotational octahedral distortions condense in addition to the initial tetragonal displacements when lowering the temperature. They

further reduce the symmetry from tetragonal to orthorhombic, monoclinic, triclinic, and finally to a second monoclinic phase. A structural sequence, which contains phases stabilized by temperature, is given in Fig. 1. A monoclinic phase ($P2_1/n$) [21] and a triclinic phase $P\bar{1}$ exist at room temperature [25,26]. At higher temperatures, Vogt *et al.* [22] and Locherer *et al.* [19] concluded a transition from $Pbcn$ to the $P4/ncc$ phase and Howard *et al.* [23] observed an intermediate $P2_1/c$ phase. Locherer *et al.* [19] and Woodward *et al.* [26] found an additional transition from $P4/ncc$ to $P4/nmm$ at 980 to 1200 K. Below room temperature, Salje *et al.* [20] reported a transition from the triclinic $P\bar{1}$ phase to a polar phase (Pc) with no further transitions down to 5 K.

WO₃ occurs (almost) always as oxygen deficient WO_{3-x} with a metal-insulator transition to a metallic phase for high concentrations of oxygen vacancies or doping with alkali metals. Superconductivity occurs in the metallic phase [9] even if the reduced regions are restricted to nanoscale twin boundaries. Bulk superconductivity in WO_{3-x} was found in a tetragonal phase with space group $P\bar{4}2_1m$ [10]. (Bi-) polaronic electron transport is a characteristic property of WO_{3-x} [31–34].

Numerous first-principles studies were performed on WO₃ in order to characterize its electronic structure (bulk, thin films, and cluster phases [35–41]), the role of oxygen vacancies [42–45], and cation doping [46–53]. In this paper we do not only focus on the electronic structure but also extensively study the structural stabilities and metastabilities of the various phases. We show that the hybrid functional B1-WC is preferable for the study of the electronic and structural properties of WO₃ over previous approaches. In the first section we check the validity of the B1-WC functional against six known crystallographic phases. The sole disagreement exists for the crystallographic ε phase (Pc), which yields a higher symmetric $P2_1/c$ structure. In the second section we analyze metastable phases starting from the phonon
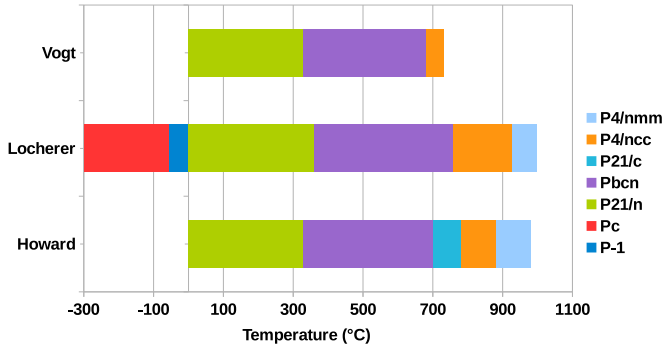
FIG. 1. Schematic summary of the temperature phase diagram WO$_3$ as reported by three main experimental sources (Vogt *et al.* from Ref. [22], Locherer *et al.* from Ref. [21], and Howard *et al.* from Ref. [23]).

dispersions of the hypothetic cubic phase, identifying the main phonon instabilities. We then condense various possible combinations of these unstable modes in order to reproduce all experimentally observed structures. This procedure also reveals two new polar phases that are close in energy to the ground-state.

II. COMPUTATIONAL DETAILS

Our first-principles calculations have been performed in the context of density functional theory, using the B1-WC hybrid functional [54] as implemented in the CRYSTAL code [55]. We have used the all-electron double-ζ basis sets for the oxygen atoms and small core Detlev Figgen pseudopotentials [56], associated with double-ζ valence basis sets for tungsten. We performed full structural relaxations with a convergence criteria on the root-mean square of the gradient and displacements smaller than 5×10^{-4} hartree/bohr and 5×10^{-4} bohrs, respectively. The electronic self-consistent calculations were converged until the difference of the total energy was smaller than 10^{-9} hartree. The phonon frequencies and Born effective charges were computed using frozen phonon numerical differences [57,58] and the electric polarization through the Berry phase technique [59]. The integration in the Brillouin zone has been performed with a $8 \times 8 \times 8$ grid of k points for the cubic unit cell and a $4 \times 4 \times 4$ grid for cells doubled in the three directions with respect to the cubic one.

Our choice of a hybrid functional is in line with the results of Wang *et al.* [44], who have shown that hybrid functionals, and especially HSE06, provide good description of the structural and electronic properties of WO$_3$. In our study, we selected the B1-WC functional that was specially designed for perovskite oxides [54] and was already successfully applied to a variety of other compounds [60–63].

III. ANALYSIS OF THE EXPERIMENTAL PHASES

Several density functional theory (DFT) studies of WO$_3$ have been performed previously [37,38,41–44,46–52,64] essentially focusing on the main and most common phases and on the electronic structure analysis with and without oxygen vacancies. A detailed analysis of the complex structural phase diagram of WO$_3$ is thus missing while a microscopic

knowledge of the origin of these different phases would be extremely valuable to understand the unique properties of WO$_3$.

In this section we start by characterizing the different phases of WO$_3$ observed experimentally to validate our approach and we will discuss the possible origin of the Pc phase. We will also analyze the electronic structure of these phases and we will discuss how the B1-WC compares with the previous studies. Further analysis of these phases and other never observed metastable phases (comparison of relative internal energies, symmetry mode analysis of the distortions, coupling of modes) will be reported in Sec. IV B).

A. Structural and crystallographic analysis

In Table I we compare our calculated crystallographic data of the $P4/nmm$, $P4/ncc$, $Pbcn$, $P2_1/n$, $P\bar{1}$, and $P2_1/c$ phases against the experimental measurements. Because the $P2_1/c$ phase is not observed experimentally at low temperature, we compare it with the closely related experimental Pc phase.

Our calculations of the $P4/nmm$ phase are in very good agreement with the observed cell parameters and the atomic positions. The $P4/nmm$ phase is antipolar and consists of highly distorted WO$_3$ octahedra where the W–O bonds dimerize in opposite direction along the [110] perovskite direction. This W–O dimerization forms local dipole moments that are aligned along the [001] direction and antialigned along the [110] direction, so that the total dipole moment cancels. The crystallographic unit cell is elongated along the [001] direction and compressed along the [100] and [010] directions. This antipolar distortion remains present in all the phases discussed below in this section.

The $P4/ncc$ phase shows additional octahedra rotations around the z axis ($a^0a^0c^-$ in the Glazer notation [65]), which induces a cell doubling along the [001] direction. The calculated c cell parameter and the z component of the atomic positions are in good agreement with experiments while the in-plane displacements are less well reproduced (Table I). The calculated a and b cell parameters are smaller than in experiments by 0.1 Å and the deviation from the tetragonal O$_2$ position is about two times larger than observed. We clearly overestimate the amplitude of the $a^0a^0c^-$ distortion (rotation angle of 13° instead of 7°; see also Fig. 7 further discussed in Sec. IV B). Although this could be partly intrinsic to the functional [66], it is worth noticing that our calculations ignore thermal effects while experiments were performed at high temperatures at which distortions might be reduced [67]. Although such a reduction does not seem to appear for the antipolar motions in the $P4/nmm$ and $P4/ncc$ phases, it might be more substantial for the rotations and we observe that the computed amplitudes of out-of-phase rotations are in much better agreement with experimental data for the low-temperature phases (see further discussed in Sec. IV B).

The orthorhombic $Pbcn$ phase can be characterized by an additional in-phase octahedra rotation about the crystallographic y axis, yielding a rotation pattern $a^0b^+c^-$. We find a similar overestimate of the octahedra distortions as for the $P4/ncc$ phase while the calculated cell parameters are underestimated with respect to experiments. We note that

TABLE I. Calculated lattice parameters in Å and Wyckoff positions of distorted WO_3 phases fully relaxed with the B1-WC functional. For each phase, we specify the space group and the experimental parameters are reported for comparison.

$P4/nmm$	Present			Exp. [23]		
	a	b	c	a	b	c
	5.299	5.299	3.930	5.297	5.297	3.929
	x	y	z	x	y	z
W_1 (2c)	1/4	1/4	−0.0640	1/4	1/4	−0.0660
O_1 (2c)	1/4	1/4	0.4900	1/4	1/4	0.4900
O_2 (4d)	0	0	0	0	0	0
$P4/ncc$	Present			Exp. [23]		
	a	b	c	a	b	c
	5.168	5.168	7.870	5.278	5.278	7.849
	x	y	z	x	y	z
W_1 (4c)	1/4	1/4	0.2849	1/4	1/4	0.2832
O_1 (4c)	1/4	1/4	0.0057	1/4	1/4	0.0030
O_2 (8f)	0.0570	−0.0570	1/4	0.0250	−0.0250	1/4
$Pbcn$	Present			Exp. [22]		
	a	b	c	a	b	c
	7.284	7.528	7.684	7.333	7.573	7.740
	x	y	z	x	y	z
W_1 (3d)	0.2510	0.0260	0.2800	0.2520	0.0290	0.2830
O_1 (3d)	−0.0010	0.0430	0.2150	−0.0020	0.0320	0.2210
O_2 (3d)	0.2930	0.2590	0.2590	0.2830	0.2690	0.2590
O_3 (3d)	0.2870	0.0100	0.0060	0.2800	0.0130	0.0020
$P2_1/n$	Present			Exp. [23]		
	a	b	c	a	b	c
	7.359	7.486	7.544	7.303	7.538	7.692
	α	β	γ	α	β	γ
	90°	91.311°	90°	90°	90.855°	90°
	x	y	z	x	y	z
W_1 (4e)	0.2720	0.0074	0.2790	0.2528	0.0260	0.2855
W_2 (4e)	0.2270	0.0133	0.7750	0.2497	0.0344	0.7805
O_1 (4e)	0.0043	0.0410	0.2165	0.0003	0.0337	0.2122
O_2 (4e)	−0.0056	0.4576	0.2170	−0.0011	0.4632	0.2177
O_3 (4e)	0.2883	0.2534	0.2924	0.2843	0.2598	0.2852
O_4 (4e)	0.2029	0.2530	0.7198	0.2080	0.2588	0.7332
O_5 (4e)	0.2795	0.0385	0.0059	0.2856	0.0410	0.0041
O_6 (4e)	0.2790	0.4630	−0.0047	0.2841	0.4868	−0.0056
$P\bar{1}$	Present			Exp. [25]		
	a	b	c	a	b	c
	7.334	7.446	7.612	7.309	7.522	7.678
	α	β	γ	α	β	γ
	88.652°	91.022°	91.012°	88.810°	90.920°	90.930°
	x	y	z	x	y	z
W_1 (2i)	0.2603	0.0172	0.2826	0.2566	0.0259	0.2850
W_2 (2i)	0.2540	0.5210	0.2183	0.2502	0.5280	0.2158
W_3 (2i)	0.2397	0.0228	0.7793	0.2438	0.0313	0.7817
W_4 (2i)	0.2456	0.5268	0.7216	0.2499	0.5338	0.7190
O_1 (2i)	0.0015	0.0395	0.2074	0.0007	0.0386	0.2100
O_2 (2i)	0.5022	0.5406	0.2115	0.5038	0.5361	0.2181
O_3 (2i)	0.0026	0.4582	0.2897	0.0076	0.4660	0.2884
O_4 (2i)	0.5012	−0.0398	0.2906	0.4972	−0.0362	0.2878
O_5 (2i)	0.2892	0.2571	0.2836	0.2851	0.2574	0.2870
O_6 (2i)	0.2081	0.7575	0.2174	0.2204	0.7630	0.2223
O_7 (2i)	0.2098	0.2569	0.7232	0.2186	0.2627	0.7258

TABLE I. (*Continued.*)

$P\bar{1}$	Present			Exp. [25]		
O_8 (2i)	0.2927	0.7575	0.7772	0.2840	0.7583	0.7679
O_9 (2i)	0.2911	0.0383	0.0060	0.2943	0.0422	−0.0002
O_10 (2i)	0.2889	0.5389	0.4941	0.2971	0.5446	0.4982
O_11 (2i)	0.2108	0.4767	−0.0061	0.2096	0.4820	−0.0072
O_12 (2i)	0.2090	−0.0242	0.5063	0.2088	0.9830	0.5051
$P2_1/c$	Present			Exp. (Pc) [20]		
	a	b	c	a	b	c
	5.263	5.150	7.618	5.278	5.156	7.663
	α	β	γ	α	β	γ
	90°	91.787°	90°	90°	91.759°	90°
	x	y	z	x	y	z
W_1 (2a)	−0.0093	−0.0173	0.6843	−0.0099	−0.0200	0.6743
W_2 (2a)	0.5011	0.4827	0.7530	0.5000	0.4710	0.7500
O_1 (2a)	0.4975	0.5769	−0.0245	0.4920	0.5780	−0.0230
O_2 (2a)	0.2087	0.2891	0.1794	0.2130	0.2890	0.1830
O_3 (2a)	0.2830	0.7891	0.2580	0.2830	0.7860	0.2590
O_4 (2a)	0.6999	0.2090	0.1795	0.7050	0.2070	0.1820
O_5 (2a)	0.7918	0.7090	0.2579	0.7960	0.7110	0.2610
O_6 (2a)	−0.0058	0.0769	0.4630	−0.0058	0.0730	0.4616

the antipolar distortions along the z axis compare well with experiments for $P4/nmm$, $P4/ncc$, and $Pbcn$.

The $P2_1/n$ structure still contains an additional octahedra rotation around the crystallographic x axis, yielding a rotation pattern $a^-b^+c^-$. The calculated cell volume is slightly too small ($+0.7$, -0.7, and -1.9% for a, b and c cell parameters respectively) and the oxygen motions related to the octahedra tilt are overestimated (Table I).

The $P\bar{1}$ phase is similar to the $P2_1/n$ phase if one replaces the in-phase rotation by an out-of-phase rotation, yielding a rotation pattern $a^-b^-c^-$. The distortions are anisotropic in all three directions, which causes the cell to be triclinic with the angles α, β, and γ close to 90°. The calculated a, b, and c cell parameters deviate from experiments by $+0.4$, -1.1, and -0.8%, respectively.

The $P2_1/c$ differs from the $P\bar{1}$ by the fact that two out-of-phase rotations have the same amplitudes, yielding a rotation pattern $a^-a^-c^-$. This phase was never reported at low temperatures but is closely related to the experimental ε (Pc) phase, which only differs from the $P2_1/c$ phase by an additional polar distortion along the c axis. While relaxing the low-temperature Pc phase, we observed that the system always comes back in to the higher $P2_1/c$ symmetry. Wijs *et al.* using local-density approximation and generalized gradient approximation exchange-correlation functionals [38] found a similar effect. To further assess the dynamical stability of the $P2_1/c$ phase with respect to a potential Pc ground state, we computed the zone-center phonons and did not observe any unstable mode: the lowest polar mode has a frequency of 158 cm^{-1} and is far from being unstable. We also checked whether a soft polar mode can be induced by increasing the cell volume but did not observe any possibility to generate a polar instability. From our calculations, the ground-state structure of intrinsic WO_3 corresponds therefore to a $P2_1/c$ phase. Following the argument by Wijs *et al.* [38], we suggest

TABLE II. Electronic band gap (in eV) of different phases of WO$_3$ as calculated in the present work with the B1-WC hybrid functional. We compare our results with previous hybrid functional calculations (PBE0, HSE06, and B3LYP), *GW* calculations, and experimental measurements.

Ref.	B1-WC	*GW* [36]	PBE0 [42]	HSE06 [42]	B3LYB [42]	Exp1 [35]	Exp2 [68]	Exp3 [43]
Cubic	1.50		2.25	1.67	1.89			
$P4/mbm$	1.27							
$I4/mcm$	1.48							
$P4/nmm$	2.12		2.28	1.71	1.85			1.75
$P4/ncc$	2.15							
Pcnb	2.65		3.35	2.57	2.89		3.21	2.35
$P2_1/n$	2.85	2.90	3.67	2.80	3.13	2.75	3.25	2.60
$P\bar{1}$	2.98	3.00	3.67	2.94	3.17			
P2$_1$/c	3.28	3.30						

FIG. 2. Calculated density of states of the $P\bar{1}$, $P2_1/n$, and $P2_1/c$ phases with the B1-WC functional.

that the polarity in the experimental ε (Pc) phase may be stabilized by the presence of oxygen vacancies or by another extrinsic parameter.

In Table I we compare our calculated atomic positions and cell parameters of the $P2_1/c$ phase with the experimentally determined Pc phase. The deviations are surprisingly small for lattice parameters ($+0.2$, -0.2, and -0.5% for a, b, and c) and even smaller for the atomic positions. Comparing the structural parameters obtained with other hybrid functionals PBE0, B3LYP, and HSE06 reported by Wang *et al.* [42], we find close agreement with a typical smaller error margin for B1-WC. B1-WC gives a much better agreement for the $P2_1/c$ phase with experimental data than using the three hybrid functionals tested by Wang *et al.* : HSE06, B3LYP, and PBE0 with errors of $+0.6$, $+1.3$, and $+0.2\%$ on a; $+2.1$, $+2.5$, and $+0.6\%$ on b; and $+0.1$, $+3.0$, and $+1.7\%$ on the c parameter. We notice, however, that the B1-WC often underestimates cell parameters while the three other hybrid functionals overestimate the cell parameters of WO$_3$.

B. Electronic structure

In Table II we compare the calculated electronic structures for the hypothetical cubic, $P4/nmm$, $P4/ncc$, $Pbcn$, $P2_1/n$, $P\bar{1}$, and $P2_1/c$ phases and compare them with the experiments and previous DFT calculations using PBE0, HSE06, and B3LYP hybrid functionals and *GW*. For the $P2_1/n$ and $P\bar{1}$ phases, experimental data coincide with the B1-WC band gaps. The B1-WC results are similar to those obtained with the HSE06 functional while the PBE0 gives a slightly smaller gap energy and B3LYP larger values. The B1-WC band gap is closest to the results of *GW* calculations, an agreement also observed for the $P2_1/c$ phase.

Comparing the trend of band gaps between the different phases, we find that both the appearance of antipolar motions in the $P4/nmm$ phase and out-of-phase rotations in the $I4/mcm$ significantly open the band gap with respect to the cubic phase. Only the in-phase rotations in the $P4/mbm$ phase seem to play a more minor role and slightly close the band gap. The calculated electronic gaps are in reasonable agreement with the experimental values for the three low-temperature structures:
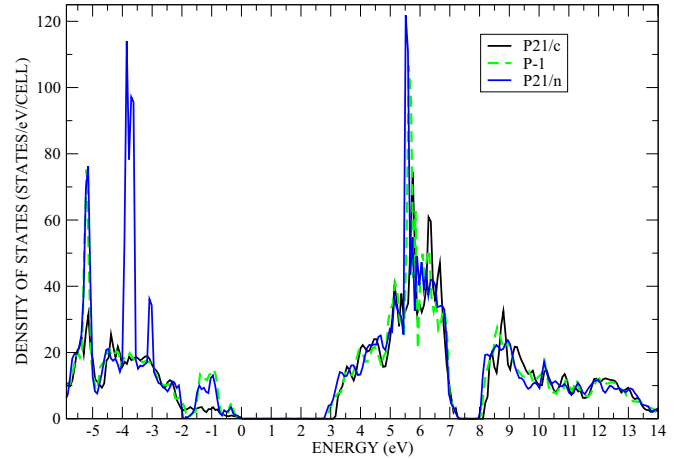
$Eg = 2.85$ eV for the room-temperature monoclinic phase $P2_1/n$, $Eg = 2.98$ eV for the triclinic phase $P\bar{1}$, and $Eg = 3.28$ eV for the monoclinic phase $P2_1/c$. Figure 2 shows the density of states of these three phases to demonstrate their similarity.

IV. ORIGIN OF THE WO$_3$ PHASES

The results presented so far give us confidence that the B1-WC functional reproduces well the experimental measurements so that we can now focus on the structural instabilities of the hypothetical $Pm\bar{3}m$ cubic parent phase and explain how their condensation gives rise to the various known phases of WO$_3$. This also allows us to identify novel ferroelectric metastable phases. In each case, we analyze the crystallographic structure through a decomposition of the distortions with respect to the cubic parent phase in terms of symmetry-adapted modes.

A. Unstable modes of the cubic reference

Figure 3 shows the calculated phonon dispersion curves of hypothetical cubic WO$_3$. Two branches of instabilities (imaginary frequencies plotted as negative numbers in Fig. 3) coexist in the Brillouin zone.

The first unstable branch has its largest imaginary value at Γ. The Γ unstable mode has the irreducible representation (irrep) Γ_4^- and corresponds to a polar mode. It suggests that the cubic phase of WO$_3$ is mostly unstable via this polar instability and might be ferroelectric, which we will see later is not exactly the case. The polar instability at Γ propagates toward the X and M points with weak dispersion while it strongly disperses towards the R point. Aside from Γ, the modes of this branch are antipolar. The dispersion of this unstable branch is very similar to the one reported in BaTiO$_3$ and corresponds to a ferroelectric instability requiring a chainlike correlation of displacements in real space [70].

The second branch of unstable modes appears between M and R points with smaller amplitudes and a nearly absent dispersion between these two points. The labels of the M and R point unstable phonon modes are M_3^+ and R_4^+ and
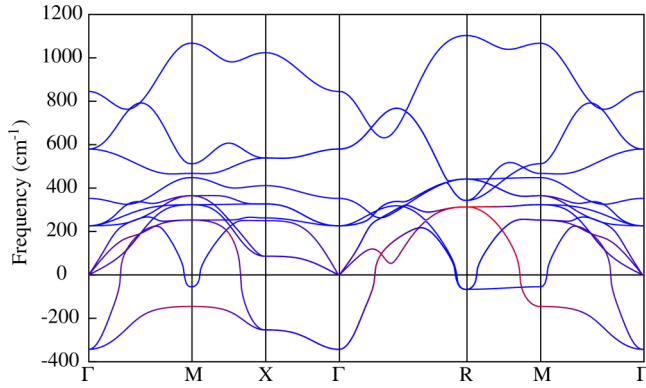
FIG. 3. Phonon dispersion curves of cubic WO$_3$ (negative frequencies refer to imaginary frequencies, i.e., to unstable modes). The coordinates of the high-symmetry points are as follows: Γ (0,0,0), X ($\frac{1}{2}$,0,0), M ($\frac{1}{2}$,$\frac{1}{2}$,0), and R ($\frac{1}{2}$,$\frac{1}{2}$,$\frac{1}{2}$). Thanks to the *band2eps* postprocessing script of ABINIT [69], the color of the bands is assigned to each point through the contribution of each atom type to the corresponding eigenvector: red for the tungsten atom and blue for the oxygens.

they correspond to rotations of the oxygen octahedra. The dispersion of this branch is comparable to what is observed for similar modes in SrTiO$_3$ or PbTiO$_3$ and linked to a planar character of the correlations of the atomic displacements in real space [70].

Figure 4 represents a schematic view of the eigenvectors related to the main instabilities of cubic WO$_3$. The polar mode at Γ (Γ_4^-, $373i$ cm^{-1}) shows motion of W against the O atoms, which is the source of a large electrical polarization. The antipolar modes at the X (X_5^-, $256i$ cm^{-1}) and M points (M_3^-, $147i$ cm^{-1}) are associated to opposite displacements from unit cell to unit cell along the [100] and [110] directions, respectively [71]. The M_3^+ ($62i$ cm^{-1}) and R_4^+ ($69i$ cm^{-1}) unstable modes correspond rotations of the oxygen octahedra about the central W atom with consecutive octahedra along the rotation direction moving, respectively, in the same or opposite directions. Using the Glazer notation [65], the M_3^+ mode corresponds to $a^0a^0a^+$ and the R_4^+ mode corresponds to $a^0a^0a^-$.

B. Condensation and coupling of modes

Starting from the previous unstable modes, we now investigate how their individual and combined condensations in the hypothetical cubic structure give rise to various phases. We then compare their energies and analyze the amplitudes of distortions.

1. Condensation of modes of the unstable polar branch

We first consider the condensation of unstable Γ_4^-, X_5^-, and M_3^- modes. Figure 5 shows the energy gain of the corresponding relaxed phase with respect to the cubic phase. We tested several condensation schemes: (i) condensation of the polar Γ_4^- mode along one ($P4mm$), two ($Amm2$), and three ($R3m$) directions; (ii) condensation of the X_5^- along one ($Pmma$) and two ($P2_1/m$) directions; and (iii) condensation of the M_3^- mode along one direction ($P4/nmm$).

Γ_4^-

M_3^-

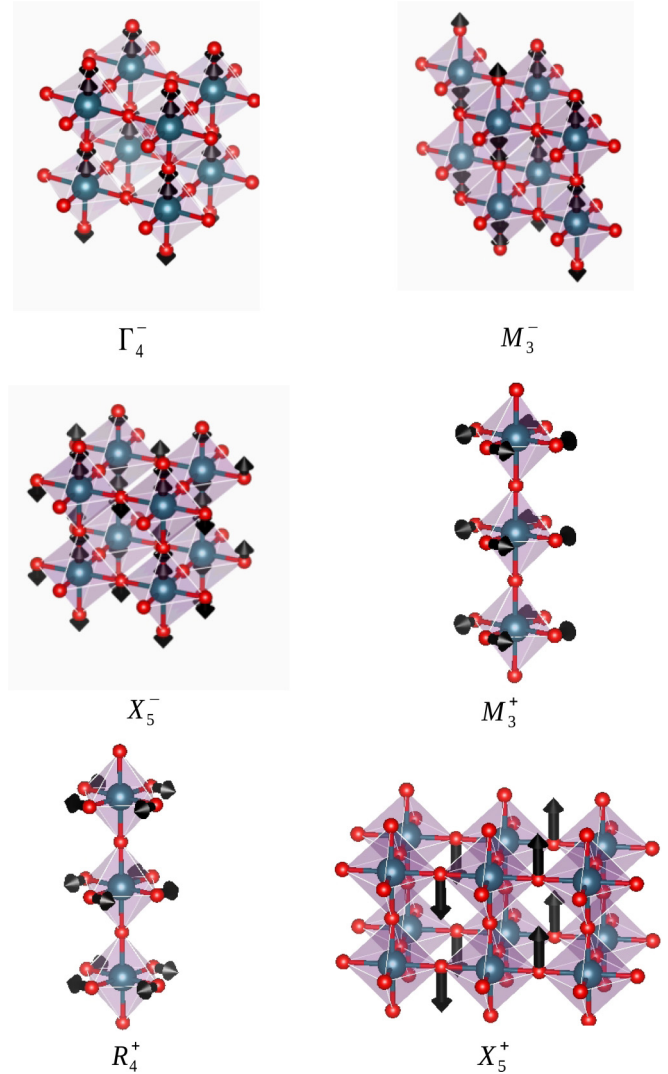X_5^-

M_3^+

R_4^+

X_5^+

FIG. 4. Schematic view of the most important modes contributing to the distortions of WO$_3$. Small red spheres represent the oxygens, and large blue spheres represent the tungsten atoms. All the modes are unstable but the X_5^+ mode, which is discussed in Sec. IV B 4.

We observe that the energy gain of the polar instabilities is large and that the Γ_4^- polar mode drives a larger gain of energy (red columns in Fig. 5) than the antipolar X_5^- and M_3^- modes (green columns in Fig. 5). The space group related to the condensation of the M_3^- mode corresponds to the high-temperature phase observed experimentally ($P4/nmm$).

Condensation of the Γ_4^- mode along two and three directions produces energy gains larger than its condensation in a single direction so that the Γ_4^- mode alone will drive the system polar along the [111] direction with an energy difference between the $Amm2$ and $R3m$ phases of 6 meV. We calculated the polarization amplitude in the three $P4mm$, $Amm2$, and $R3m$ phases using the Berry phase technique and obtain 54, 69, and 69 μC cm^{-2}. These polarization values are comparable to those observed in robust ferroelectrics such as PbTiO$_3$. They can be explained by the opposite motions of W and O atoms, associated with strongly anomalous Born effective charges (11.73 e for W and $-8.78/-1.62$ e for O$_\parallel$/O$_\perp$ in good agreement with previous calculations in Ref. [72]).

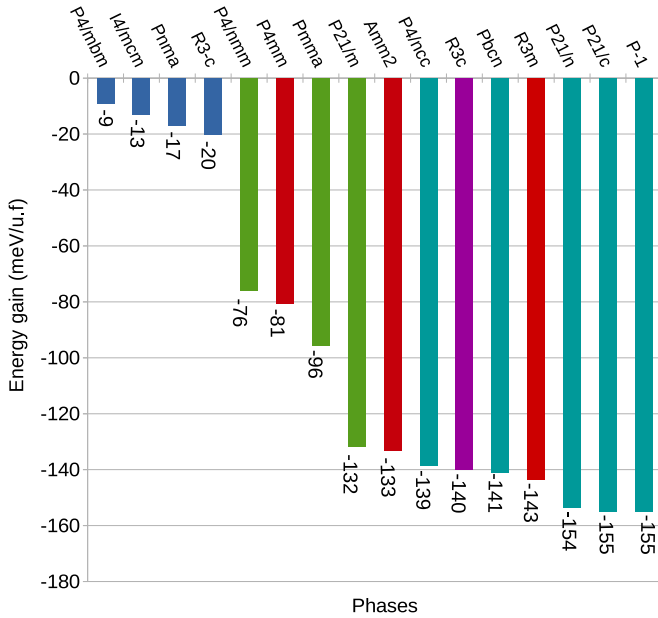FIG. 5. Calculated energy gain (in meV/f.u.) with respect to the cubic phase of different phases of WO_3. Red columns are the FE phases arising for the condensation of the polar unstable mode, blue columns are the phases arising from the condensation of the oxygen octahedral rotation unstable modes, green columns are the phases arising from the condensation of antipolar modes, the magenta column represents a phase combining FE and antipolar modes, and cyan columns represent phases combining oxygen octahedral rotations and antipolar modes. For clarity, the exact value of the energy gain is written in each case.

2. Condensation of modes of the oxygen rotation unstable branch

Figure 5 (blue columns) shows the energy gain given by the condensation of the M_3^+ and R_4^+ modes along one direction ($I4/mbm$ and $I4/mcm$), the R_4^+ mode in three directions ($R\bar{3}c$), and the orthorhombic $Pnma$ phase where the R_4^+ mode is condensed in two directions and the M_3^+ mode in one direction ($a^-a^-c^+$). These distortions lower the energy much less than the polar and antipolar motions. This observation is in line with the modest amplitude of the related phonon instabilities: the energy curvatures at the origin are less negative for the octahedral rotations than for the polar motion. Nevertheless the amplitudes of octahedral rotations are 10.7 and 11.7 deg in $I4/mbm$ and $I4/mcm$, respectively. Such large distortions associated to a weak instability highlight relatively small anharmonicities, which might be explained by the absence of the A cation with respect to regular ABO_3 perovskites [73].

3. Combinations of modes

Beside the $P4/nmm$ phase, none of the previous single irrep mode condensations correspond to observed phases. Thus, we now explore the condensation of combined octahedral rotations and polar/antipolar modes. We depict in Fig. 5 the energy gain given by the joint condensation of polar and oxygen rotation modes along three directions ($R3c$, in purple color) and of antipolar and oxygen rotation modes ($P4/ncc$, $Pbcn$, $P2_1/n$, $P2_1/c$, and $P\bar{1}$, in cyan color).

Combining the polar distortion of the low-energy $R3m$ phase with additional oxygen rotation modes does not further reduce the energy. Instead, it yields a $R3c$ phase slightly higher in energy but with a slightly amplified polarization of 71 $\mu C\,cm^{-2}$ and a slightly reduced oxygen rotation (with respect to the $R\bar{3}c$). This emphasizes an unusual competition between these two types of distortions in WO_3 with respect to regular perovskite compounds, where in WO_3 the $R3c$ phase forms a local minimum between the $R\bar{3}c$ and $R3m$ phases.

At the opposite, the mixing of the antipolar mode M_3^- with oxygen rotation modes can drive larger energy gains so that the ferroelectric $R3m$ phase is not the ground state. This is in agreement with experimental observations where the observed phases at all temperatures contain antipolar motions. Among investigated phases, the $P2_1/c$ phase appears as the most stable but only marginally, as we observe that the $P2_1/n$, $P2_1/c$, and $P\bar{1}$ phases are all extremely close in energy (energy gains of 153, 155, and 155 meV, respectively, see Fig. 5). Consequently, within the precision of our calculations, we cannot unambiguously assess which one is the ground state. Nevertheless, as discussed in Sec. III A and further exemplified in the next section, the $P2_1/c$ phase is in excellent agreement with the experimental Pc ground state, except for a tiny polar distortion. Our calculations highlight that, in fact, the $P2_1/n$ and $P\bar{1}$ phases observed at higher temperatures are also extremely close in energy.

We further notice that the ferroelectric $R3m$ phase, although never observed experimentally, is also relatively close in energy to the ground state (about 11 meV/f.u.). Following Rabe [74], the nonpolar (or eventually weakly polar in the experimental Pc phase) ground state of WO_3 combined with an alternative low-energy ferroelectric phase obtained by polar distortions of the same high-symmetry reference structure makes it a potential antiferroelectric compound. Indeed, applying an electric field, it might be possible to open a typical double hysteresis loop from a field-induced first-order transition from the $P2_1/c$ ground state to the $R3m$ polar phase. Estimating the critical electric field required to stabilize the $R3m$ phase from $\mathcal{E}_c \sim \Delta E/\Omega_0 P_s$ [75], where ΔE is the energy difference between the two phases (11.43 meV/f.u.), P_s is the spontaneous polarization of the polar phase (69 $\mu C\,cm^{-2}$), and Ω_0 is its unit-cell volume (55 Å), we get the relatively modest value $\mathcal{E}_c \sim 480$ kV/cm. For the polar phase $R3c$ we need to apply a greater electric field $\mathcal{E}_c \sim 638$ kV/cm to stabilize this phase. This allows us to estimate that the critical field has similar value with respect to other antiferroelectric material, $\mathcal{E}_c \sim 470$ kV/cm for ZrO_2 [75] and $\mathcal{E}_c \sim 239$ kV/cm for $PbZrO_3$ [76]. Although this might not be easy to check experimentally on real samples that are typically oxygen deficient and highly conductive, the calculations reveal that stoichiometric WO_3 exhibits all the features of an antiferroelectric compound.

4. Symmetry adapted mode analysis of the distorted phases

To quantify the distortions that appear in the various phases we project the structural distortions onto symmetry adapted modes of the cubic phase using AMPLIMODE software [77]. The results in Fig. 6 show the amplitudes of the modes in the fully relaxed phases from the calculations but nonobserved
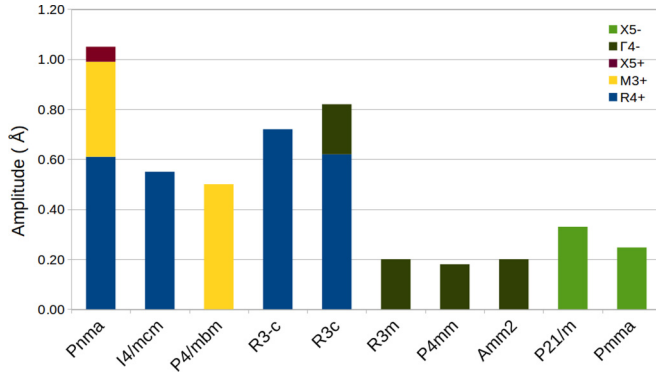
FIG. 6. Symmetry adapted mode decomposition of distorted phases of WO₃ explored in our study but not observed experimentally.

experimentally. In Fig. 7 we show the amplitudes of modes in both the fully relaxed and observed phases, which can be compared.

In the following we discuss the competition or cooperation character of the mode distortions. In perovskite oxides, it is established that the oxygen rotations are in competition with the ferroelectric displacements but less attention has been given to the combinations of other types of mode. Often, this cooperation or competition comes from the biquadratic energy term in the free-energy expansion with respect to two order parameters. In WO₃, we observe that the combination between the Γ_4^- mode and the R_4^+ mode along the [111] direction in the $R3c$ phase has the tendency to reduce the amplitude of the oxygen rotations with respect to the $R\bar{3}c$ phase (the R_4^+ mode is 13% smaller in the $R3c$ phase than in the $R\bar{3}c$ phase, see Fig. 6) while the polar mode is unaffected. As discussed in the previous section, the combination of the Γ_4^- and R_4^+ modes forms a local minimum ($R3c$ phase) of higher energy than the $R3m$ phase. This means that the polar distortions are in competition with the oxygen rotations as reported for perovskite oxides, with the difference that the polar mode amplitude is unaffected and that the $R3c$ phase is locally
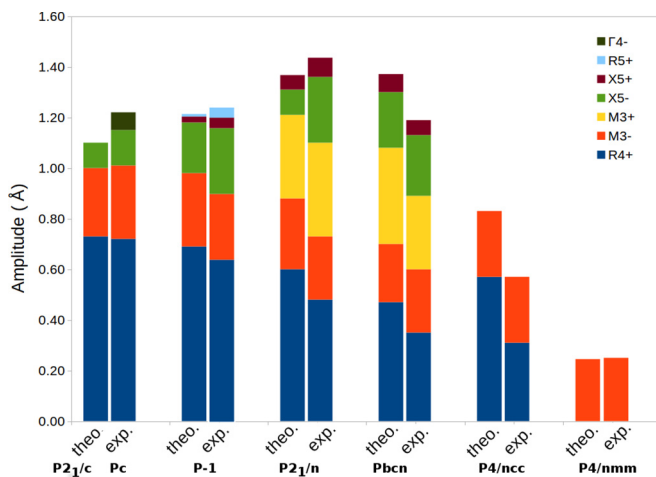
stable (the system does not relax into the lowest-energy $R3m$ phase). The strain can also play an important role [78], but when performing the same calculations at fixed cell parameters (fixed to the cubic ones), we find that the $R3c$ phase still forms a local minimum of higher energy than the $R3m$ phase. This unusual energy landscape can come from the marginal gain of energy of the oxygen rotations while large amplitudes of rotations are present.

On the other hand, the association of the oxygen rotations with the antipolar M_3^- mode is cooperative. When we compare the amplitude of the R_4^+ and M_3^- modes of the $P4/nmm$, $I4/mcm$, and $P4/ncc$ (Figs. 6 and 7) we find that when both the R_4^+ and M_3^- modes are present together in the $P4/ncc$ phase, their amplitude is slightly higher (4% larger) than when condensed alone ($P4/nmm$ and $I4/mcm$ phases). Their combination, however, drives a sizable gain of energy: the $P4/ncc$ phase is 63 and 126 meV lower in energy than the $P4/nmm$ and the $I4/mcm$ phases, respectively. This means that the combination of the oxygen rotations with the antipolar M_3^- mode is much more cooperative than the combination with the polar mode Γ_4^-.

The $Pbcn$ phase can be understood as a distorted $P4/ncc$ phase with additional M_3^+ oxygen rotations along [010]. The resulting tilt pattern is $a^0 b^+ c^-$ with a small energy gain of 2 meV with respect to the $P4/ncc$ phase and a reduction of mode amplitudes M_3^-, R_4^+, and M_3^+ (16, 7, and 22% reduction of the M_3^-, R_4^+, and M_3^+ modes with respect to the phases where they are condensed alone, i.e., $P4/nmm$, $I4/mcm$, and $P4/mbm$, respectively). The M_3^+ mode competes with the R_4^+ and M_3^- modes in the sense their combination reduces their amplitude, but they cooperate to lower the energy of the system.

In the case of the monoclinic $P2_1/n$, $P2_1/c$, and triclinic $P\bar{1}$ phases, the combination of the M_3^- mode with several oxygen rotations ($a^- b^+ c^-$ for $P2_1/n$, $a^- a^- c^-$ for $P2_1/c$, and $a^- b^- c^-$ for $P\bar{1}$) lowers the energy of the crystal and with an increase of the mode amplitude with respect to the phases where these modes are condensed independently. For example, the antipolar M_3^- mode has his amplitude increased by 11, 10, and 19% in the $P2_1/n$, $P2_1/c$, and $P\bar{1}$ phases, respectively. This means that the dominant R_4^+ oxygen rotations cooperate with the antipolar M_3^- mode to promote the ground state of WO₃.

We note that in the $P4/nmm$, $P4mm$, $Amm2$, $R3m$, $I4/mcm$, $I4/mbm$, $R\bar{3}c$, $P4/ncc$, and $R3c$ phases the mode decomposition shows only the primary modes we have condensed. This is different with the $Pnma$ phase in which an additional mode X_5^+ appears with a small amplitude in the mode projections while we have condensed only the primary R_4^+ and M_3^+ modes (see Fig. 6). This additional mode appears by anharmonic coupling between the R_4^+ and M_3^+ modes such that the symmetry of the $Pnma$ structure allows the X_5^+ mode to develop even though the X_5^+ mode is not unstable by itself [79]. Similarly, we observe the apparition of several additional modes in the $Pbcn$, $P2_1/n$, $P2_1/c$, and $P\bar{1}$ phases, which we discuss in the next section.

FIG. 7. Symmetry adapted mode decomposition of distorted phases WO₃; comparison between experiments and our calculations with the B1-WC functional are shown.

5. Energy invariants

The different phases arise from the condensation of one or several unstable modes (primary modes) of the cubic parent

TABLE III. Symmetry adapted modes decomposition and linear couplings of modes of the $Pnma$, $Pbcn$, $P2_1/n$, $P2_1/c$, and $P\bar{1}$ phases. From the left to right columns, we show the mode label (Irrep.) of the symmetry adapted mode, the direction of the mode condensation, the corresponding subgroup, the amplitude of the distortion in the calculated and in the experimental cases (the modes with an amplitude lower than 0.005 Å are not shown), and the linear coupling invariants of the most relevant modes where the letters correspond to the one given in the direction column (we highlight in bold the primary modes).

Space group	Irrep.	Direction	Subgroup	Amplitudes (Å)		Linear invariants
				Calc.	Exp.	
$Pnma$	$\mathbf{R_4^+}$	$(\mathbf{a},\mathbf{a},0)$	$I4/mma$	0.61		
	$\mathbf{M_3^+}$	$(0,0,\mathbf{c})$	$P4/mbm$	0.38		$\mathbf{ab}$c
	X_5^+	$(0,a,0,0,0)$	$Cmcm$	0.06		
$Pbcn$	$\mathbf{R_4^+}$	$(0,0,\mathbf{a})$	$I4/mcm$	0.47	0.35	
	$\mathbf{M_3^+}$	$(0,\mathbf{b},0)$	$P4/mbm$	0.39	0.30	$\mathbf{ab}$e, $\mathbf{ad}$ce
	$\mathbf{M_3^-}$	$(c,0,\mathbf{d})$	$Ibam$	0.23	0.25	$\mathbf{ab}$f, $\mathbf{ad}$cf
	X_5^-	$(0,0,e,-e,0,0)$	$Pmma$	0.22	0.25	
	X_5^+	$(0,0,0,0,f,f)$	$Pmma$	0.07	0.06	
$P2_1/n$	$\mathbf{R_4^+}$	$(0,\mathbf{a},\mathbf{b})$	$C2/m$	0.60	0.48	$\mathbf{a}$eg+$\mathbf{bd}$f
	$\mathbf{M_3^+}$	$(\mathbf{c},0,0)$	$P4/mbm$	0.34	0.37	$\mathbf{ac}$h+$\mathbf{ac}$i-$\mathbf{bc}$h+$\mathbf{bc}$i
	$\mathbf{M_3^-}$	$(0,\mathbf{d},\mathbf{e})$	$Ibam$	0.27	0.25	$\mathbf{acd}$g$-\mathbf{bc}$ef
	X_5^-	$(f,-f,0,0,g,g)$	$Pmmn$	0.09	0.26	$\mathbf{ade}$h+$\mathbf{ade}$i+$\mathbf{bde}$h$-\mathbf{bde}$i
	X_5^+	$(0,0,h,i,0,0)$	$P2_1/m$	0.06	0.08	
$P2_1/c$	Γ_4^+	$(\mathbf{a},-\mathbf{a},-\mathbf{b})$	Cm	0	0.07	
	$\mathbf{R_4^+}$	$(-\mathbf{b},\mathbf{a},-\mathbf{a})$	$C2/c$	0.73	0.72	$\mathbf{ac}$d+$\mathbf{bc}$d
	$\mathbf{M_3^-}$	$(\mathbf{c},0,0)$	$P4/nmm$	0.27	0.30	
	X_5^-	$(0,0,0,-d,0,0)$	$Cmcm$	0.10	0.14	

structure but, in some cases, also include the further condensation of stable modes (secondary modes) with significant amplitudes. Often, the appearance of such secondary modes of large amplitude can be traced back in their linear coupling with the primary modes [80,81]. This can be rationalized from the existence in the energy expansion of the $Pm\bar{3}m$ phase of invariant terms of the form $\gamma Q_s \prod_{i=1}^{N} Q_p^i$ where Q_s is the amplitude of the secondary mode s and Q_p^i is the amplitude of the primary mode i. Depending of the number of primary mode involved, these coupling terms can be bilinear, trilinear, quadrilinear, etc.

To clarify the origin of secondary modes in several low-symmetry phases of WO$_3$, we restrict ourself here to the search of such multilinear invariant terms in the energy expansion around its cubic phase by using the INVARIANTS software [82]. In the last column of Table III we report these linear invariants up to the fourth order obtained for the $Pnma$, $Pbcn$, $P2_1/n$, and $P2_1/c$ phases. The letters represent the mode amplitudes (Q^i) in the directions specified in the third column where the bold letters refer to the primary modes in the structure (Q_p^i) and the normal letters refer to secondary modes (Q_s^i).

In the $Pnma$ phase, we find that the X_5^+ mode appears through a trilinear coupling with the oxygen rotations modes R_4^+ and M_3^+ ($\mathbf{ab}$c invariant in Table III). This additional X_5^+ mode is also found in $Pnma$ of ABO_3 perovskites [83,84] where the eigenvector corresponds to antipolar motions of the A cation. In WO$_3$ the A cation is absent and X_5^+ corresponds

to similar antipolar motions but of oxygen instead of the A site (see Fig. 4).

In $Pbcn$ the primary M_3^- mode condenses along z, the R_4^+ mode condenses along z, and the M_3^+ mode condenses along y and four additional secondary modes: X_5^- and X_5^+ with a large amplitude and M_5^+ and M_4^+ with a small amplitude as well as an additional component of the M_3^- mode about the x direction. If we restrict ourself to the strongest X_5^- and X_5^+ modes we find that both are coupled with the R_4^+ and M_3^+ modes through a trilinear coupling ($\mathbf{ab}$e and $\mathbf{ab}$f invariants in Table III) but also through a quadrilinear coupling with the R_4^+ mode and the two components of the M_3^- mode ($\mathbf{ad}$ce and $\mathbf{ad}$cf invariants in Table III). We can thus explain the appearance of the X_5^+ and X_5^- modes through a trilinear coupling with the oxygen octahedral rotations and the appearance of the second x component of the antipolar M_3^- mode through a coupling with the secondary X_5^+ and X_5^- modes and the primary R_4^+ mode. The final structure can thus be seen as antipolar through the M_3^- mode along z with a canting of its direction toward the x axis and through the X_5^- mode along the y direction, the whole distortions being associated with the $a^-b^+c^-$ pattern of oxygen rotation distortions.

The transition from $Pbcn$ to $P2_1/n$ can be seen as being induced by the condensation of the R_4^+ mode along the remaining direction for the oxygen rotation octahedral distortions to $a^-b^+c^-$. This means that we find the same mode coupling as in the $Pbcn$ phase plus some extra ones due to the additional mode condensation. Because we do not induce

a new irrep, the couplings are the same (i.e., trilinear and quadrilinear between the primary R_4^+, M_3^+, and M_3^- modes and the secondary X_5^- and X_5^+ modes) but in different directions from the $Pbcn$ phase: we observe the X_5^- and X_5^+ modes in two directions instead of one. Other modes also appear in the symmetry adapted mode analysis but with smaller amplitudes (M_4^+, M_5^-, M_5^+, and M_2^+), which we do not include in the invariant analysis.

$P\bar{1}$ and $P2_1/c$ are very similar in the sense that for both structures we can envisage the condensation of R_4^+ modes in three directions and the M_3^- mode in one direction. The difference is that in the $P2_1/c$ phase the R_4^+ mode is primary with the same amplitude in two directions and a different amplitude in the third direction ($a^-a^-c^-$ where the M_3^- mode is primary in the z direction) while in the $P\bar{1}$ phase the condensation of the R_4^+ mode has different amplitudes in three directions ($a^-b^-c^-$). In $P2_1/c$ the presence of the X_5^- and M_5^- secondary modes can be explained by trilinear coupling with the R_4^+ and M_3^- primary modes (**ac**d+**bc**d and **ab**e invariants in Table III) in a similar way as in the $P2_1/n$ phase.

This analysis shows that the low-symmetry phases of WO$_3$ are complex and involve numerous multilinear couplings of modes if one expands the energy with respect to the cubic phase. We note that, among possible couplings, the coupling with the secondary X_5^- mode is most important in all low-symmetry phases.

Going further, in order to test whether symmetry arguments can lead to the polar Pc phase using anharmonic couplings, we have tested if there exists any bi-, tri-, or quadri-linear coupling involving a polar mode at the Γ point. We did not find any couplings with the R_4^+, M_3^+, or M_3^- modes. We thus conclude that it is not possible to generate polarity in WO$_3$ in the limit to these primary modes, which are the ones appearing in other experimental phases.

V. CONCLUSIONS

In this study, we have performed a first-principles study of WO$_3$ using the B1-WC hybrid exchange-correlation functional which appears to yield good overall agreement with experiments regarding electronic and structural properties together.

Starting from the inspection of the phonon dispersion curves of a hypothetical cubic structure taken as reference, we have identified two main branches of instabilities and characterized various phases arising from the condensation of one or more unstable modes. Although the dominant phonon

instability is associated to a zone-center polar mode, we found a nonpolar $P2_1/c$ ground state arising from the combination of cooperative antipolar distortions and oxygen octahedra rotations. This phase is very similar to the experimentally reported polar Pc ground state, except for the absence of a tiny polar distortion. Our calculations do not show, however, any tendency of the $P2_1/c$ phase to evolve to a Pc phase suggesting that WO$_3$ is likely not intrinsically ferroelectric. Instead the ferroelectric character might arise from extrinsic defects such as oxygen vacancies. The $P2_1/c$ phase is antipolar and defects could easily produce a slightly unbalanced antidipole structure, yielding a weak net polarization. In this sense, off-stoichiometric WO$_3$ might be better described as a *ferrielectric* compound [85]. The ground state is determined by two antiparallel movements of W off-centerings which exactly compensate each other in the $P2_1/c$ phase. The displacements are almost identical in the Pc phase, but the two displacements do not fully compensate each other. We suspect that such weak ferrielectricity can be induced by defects such as oxygen vacancies.

At the level of our calculations, the $P2_1/c$ ground state is almost degenerated in energy with the $P2_1/n$ and $P\bar{1}$ phases observed at higher temperature. Also, we discovered the existence of a never observed and low-energy ferroelectric $R3m$ phase with a large polarization. Although this might not be of direct interest due to the conductive character of usual off-stoichiometric samples, the proximity with the $P2_1/c$ ground state of this structurally unrelated $R3m$ polar phase toward which the system could be switched through a first-order transition under moderate electric fields makes WO$_3$ a potential antiferroelectric material.

[1] E. Salje, Opt. Commun. **24**, 231 (1978).

[2] G. A. Niklasson and C. G. Granqvist, J. Mater. Chem. **17**, 127 (2007).

[3] S. K. Deb, Solar Energy Materials and Solar Cells **92**, 245 (2008), selected Papers from the Seventh International Meeting on Electrochromism (IME-7) Seventh International Meeting on Electrochromism.

[4] R. Baetens, B. P. Jelle, and A. Gustavsen, Solar Energy Materials and Solar Cells **94**, 87 (2010).

[5] S.-H. Lee, R. Deshpande, P. Parilla, K. Jones, B. To, A. Mahan, and A. Dillon, Adv. Mater. **18**, 763 (2006).

[6] A. Subrahmanyam and A. Karuppasamy, Solar Energy Materials and Solar Cells **91**, 266 (2007).

[7] C. Sella, M. Maaza, O. Nemraoui, J. Lafait, N. Renard, and Y. Sampeur, Surf. Coat. Technol. **98**, 1477 (1998), papers presented at the Fifth International Conference on Plasma Surface Engineering.

[8] Y. Zhao, Z. C. Feng, Y. Liang, and H. W. Sheng, Appl. Phys. Lett. **71**, 2227 (1997).

[9] A. Aird and E. K. H. Salje, J. Phys.: Condens. Matter **10**, L377 (1998).

[10] A. Aird, M. C. Domeneghetti, F. Mazzi, V. Tazzoli, and E. K. H. Salje, J. Phys.: Condens. Matter **10**, L569 (1998).

[11] E. Salje, Ferroelectrics **12**, 215 (1976).

[12] A. Shengelaya, S. Reich, Y. Tsabba, and K. Müller, The European Physical Journal B **12**, 13 (1999).

[13] V. Barzykin and L. P. Gorkov, Phys. Rev. Lett. **89**, 227002 (2002).

[14] Y. Kim, M. Alexe, and E. K. H. Salje, Appl. Phys. Lett. **96**, 032904 (2010).

[15] C. G. Granqvist, Solar Energy Materials and Solar Cells **60**, 201 (2000).

[16] Dane T. Gillaspie, Robert C. Tenent, and Anne C. Dillon, J. Mater. Chem. **20**, 9585 (2010).

[17] E. Salje and K. Viswanathan, Acta Crystallographica A **31**, 356 (1975).

[18] E. Salje, Acta Crystallographica A **31**, 360 (1975).

[19] K. R. Locherer, I. P. Swainson, and E. K. H. Salje, J. Phys.: Condens. Matter **11**, 4143 (1999).

[20] E. K. H. Salje, S. Rehmann, F. Pobell, D. Morris, K. S. Knight, T. Herrmannsdörfer, and M. T. Dove, J. Phys.: Condens. Matter **9**, 6563 (1997).

[21] K. R. Locherer, I. P. Swainson, and E. K. H. Salje, J. Phys.: Condens. Matter **11**, 6737 (1999).

[22] T. Vogt, P. M. Woodward, and B. A. Hunter, J. Solid State Chem. **144**, 209 (1999).

[23] C. J. Howard, V. Luca, and K. S. Knight, J. Phys.: Condens. Matter **14**, 377 (2002).

[24] M. Boulova, N. Rosman, P. Bouvier, and G. Lucazeau, J. Phys.: Condens. Matter **14**, 5849 (2002).

[25] R. Diehl, G. Brandt, and E. Salje, Acta Crystallographica B **34**, 1105 (1978).

[26] P. Woodward, A. Sleight, and T. Vogt, Journal of Physics and Chemistry of Solids **56**, 1305 (1995).

[27] P. Woodward, A. Sleight, and T. Vogt, J. Solid State Chem. **131**, 9 (1997).

[28] S. Tanisaki, J. Phys. Soc. Jpn. **15**, 573 (1960).

[29] B. O. Loopstra and P. Boldrini, Acta Crystallogr. **21**, 158 (1966).

[30] W. L. Kehl, R. G. Hay, and D. Wahl, J. Appl. Phys. **23**, 212 (1952).

[31] O. Schirmer and E. Salje, Solid State Commun. **33**, 333 (1980).

[32] O. F. Schirmer and E. Salje, J. Phys. C **13**, L1067 (1980).

[33] E. Salje, A. Carley, and M. Roberts, J. Solid State Chem. **29**, 237 (1979).

[34] E. Salje and B. Güttler, Philosophical Magazine B **50**, 607 (1984).

[35] P. P. González-Borrero, F. Sato, A. N. Medina, M. L. Baesso, A. C. Bento, G. Baldissera, C. Persson, G. A. Niklasson, C. G. Granqvist, and A. Ferreira da Silva, Appl. Phys. Lett. **96**, 061909 (2010).

[36] M. B. Johansson, G. Baldissera, I. Valyukh, C. Persson, H. Arwin, G. A. Niklasson, and L. Österlund, J. Phys.: Condens. Matter **25**, 205502 (2013).

[37] Y. Ping, D. Rocca, and G. Galli, Phys. Rev. B **87**, 165203 (2013).

[38] G. A. de Wijs, P. K. de Boer, R. A. de Groot, and G. Kresse, Phys. Rev. B **59**, 2684 (1999).

[39] A. C. Tsipis and C. A. Tsipis, J. Phys. Chem. A **104**, 859 (2000).

[40] M. G. Stachiotti, F. Corà, C. R. A. Catlow, and C. O. Rodriguez, Phys. Rev. B **55**, 7508 (1997).

[41] F. Corà, A. Patel, N. M. Harrison, R. Dovesi, and C. R. A. Catlow, J. Am. Chem. Soc. **118**, 12174 (1996).

[42] F. Wang, C. D. Valentin, and G. Pacchioni, J. Phys. Chem. C **115**, 8345 (2011).

[43] D. B. Migas, V. L. Shaposhnikov, V. N. Rodin, and V. E. Borisenko, J. Appl. Phys. **108**, 093713 (2010).

[44] F. Wang, C. Di Valentin, and G. Pacchioni, Phys. Rev. B **84**, 073103 (2011).

[45] S. Karazhanov, Y. Zhang, A. Mascarenhas, S. Deb, and L.-W. Wang, Solid State Ionics **165**, 43 (2003), fifth International Meeting on Electrochromism.

[46] A. D. Walkingshaw, N. A. Spaldin, and E. Artacho, Phys. Rev. B **70**, 165110 (2004).

[47] S. Tosoni, C. D. Valentin, and G. Pacchioni, J. Phys. Chem. C **118**, 3000 (2014).

[48] A. Hjelm, C. G. Granqvist, and J. M. Wills, Phys. Rev. B **54**, 2436 (1996).

[49] B. Ingham, S. C. Hendy, S. V. Chong, and J. L. Tallon, Phys. Rev. B **72**, 075109 (2005).

[50] M. N. Huda, Y. Yan, S.-H. Wei, and M. M. Al-Jassim, Phys. Rev. B **80**, 115118 (2009).

[51] F. Corá, M. G. Stachiotti, C. R. A. Catlow, and C. O. Rodriguez, J. Phys. Chem. B **101**, 3945 (1997).

[52] M. N. Huda, Y. Yan, C.-Y. Moon, S.-H. Wei, and M. M. Al-Jassim, Phys. Rev. B **77**, 195102 (2008).

[53] B. Chen, J. Laverock, L. F. J. Piper, A. R. H. Preston, S. W. Cho, A. DeMasi, K. E. Smith, D. O. Scanlon, G. W. Watson, R. G. Egdell, P.-A. Glans, and J.-H. Guo, J. Phys.: Condens. Matter **25**, 165501 (2013).

[54] D. I. Bilc, R. Orlando, R. Shaltaf, G. M Rignanese, J. Íñiguez, and Ph. Ghosez, Phys. Rev. B **77**, 165107 (2008).

[55] M. Causà, R. Dovesi, C. Pisani, R. Colle, and A. Fortunelli, Phys. Rev. B **36**, 891 (1987).

[56] D. Figgen, K. A. Peterson, M. Dolg, and H. Stoll, J. Chem. Phys. **130**, 164108 (2009).

[57] F. Pascale, C. M. Zicovich-Wilson, F. López Gejo, B. Civalleri, R. Orlando, and R. Dovesi, J. Comput. Chem. **25**, 888 (2004).

[58] C. M. Zicovich-Wilson, F. Pascale, C. Roetti, V. R. Saunders, R. Orlando, and R. Dovesi, J. Comput. Chem. **25**, 1873 (2004).

[59] R. D. King-Smith and D. Vanderbilt, Phys. Rev. B **47**, 1651 (1993).

[60] M. Goffinet, P. Hermet, D. I. Bilc, and Ph. Ghosez, Phys. Rev. B **79**, 014403 (2009).

[61] A. Prikockyte, D. Bilc, P. Hermet, C. Dubourdieu, and Ph. Ghosez, Phys. Rev. B **84**, 214301 (2011).

[62] J. Varignon and Ph. Ghosez, Phys. Rev. B **87**, 140403 (2013).

[63] N. C. Bristowe, J. Varignon, D. Fontaine, E. Bousquet, and Ph. Ghosez, Nat. Commun. **6**, 6677 (2015).

[64] R. Chatten, A. V. Chadwick, A. Rougier, and P. J. D. Lindan, J. Phys. Chem. B **109**, 3146 (2005).

[65] A. M. Glazer, Acta Cryst. B **28**, 3384 (1972).

[66] P. García-Fernández, S. Ghosh, N. J. English, and J. A. Aramburu, Phys. Rev. B **86**, 144107 (2012).

[67] R. A. Cowley, Integrated Ferroelectrics **133**, 109 (2012).

[68] H. Zheng, J. Z. Ou, M. S. Strano, R. B. Kaner, A. Mitchell, and K. Kalantar-zadeh, Adv. Funct. Mater. **21**, 2175 (2011).

[69] X. Gonze et al., Comput. Phys. Commun. **180**, 2582 (2009).

[70] Ph. Ghosez, E. Cockayne, U. V. Waghmare, and K. M. Rabe, Phys. Rev. B **60**, 836 (1999).

[71] In the cubic cell, the [100], [010], and [001] directions are degenerate. The same applies for the [110], [101], and [011] directions.

[72] F. Detraux, Ph. Ghosez, and X. Gonze, Phys. Rev. B **56**, 983 (1997).

[73] N. A. Benedek and C. J. Fennie, J. Phys. Chem. C **117**, 13339 (2013).

[74] K. M. Rabe, in *Functional Metal Oxides* (Wiley, New York, 2013), pp. 221–244.

[75] S. E. Reyes-Lillo, K. F. Garrity, and K. M. Rabe, Phys. Rev. B **90**, 140103 (2014).

[76] Value calculated from the energies and polarization reported for the $R3m$ and $Pbam$ phase by S. Amisi, Ph.D. thesis, University of Liége, Belgium, 2013.

[77] D. Orobengoa, C. Capillas, M. I. Aroyo, and J. M. Perez-Mato, J. Appl. Crystallogr. **42**, 820 (2009).

[78] The volume of the cubic, $R\bar{3}c$, $R3m$, and $R3c$ phases are 54.01 Å^3, 50.89 Å^3, 55.35 Å^3, and 52.71 Å^3.

[79] J. Young, A. Stroppa, S. Picozzi, and J. M. Rondinelli, J. Phys.: Condens. Matter **27**, 283202 (2015).

[80] E. Bousquet, M. Dawber, N. Stucki, C. Lichtensteiger, P. Hermet, S. Gariglio, J. M. Triscone, and Ph. Ghosez, Nature (London) **452**, 732 (2008).

[81] N. A Benedek, J. M Rondinelli, H. Djani, Ph. Ghosez, and Ph. Lightfoot, Dalton Trans. **44**, 10543 (2015).

[82] D. M. Hatch and H. T. Stokes, J. Appl. Crystallogr. **36**, 951 (2003).

[83] N. A. Benedek, A. T. Mulder, and C. J. Fennie, J. Solid State Chem. **195**, 11 (2012).

[84] S. Amisi, E. Bousquet, K. Katcho, and Ph. Ghosez, Phys. Rev. B **85**, 064112 (2012).

[85] C. F. Pulvari, Phys. Rev. **120**, 1670 (1960).